The Astrophysical Journal, 698:1826–1837, 2009 June 20 doi:10.1088/0004-637X/698/2/1826

MICROLENSING EVENT MOA-2007-BLG-400: EXHUMING THE BURIED SIGNATURE OF A COOL, JOVIAN-MASS PLANET

Subo Dong[1,27], I. A. Bond[2,28], A. Gould[1,3,27], Szymon Kozłowski[1,27], N. Miyake[4,28], B. S. Gaudi[1], D. P. Bennett[5,28], and F. Abe[4], A. C. Gilmore[6], A. Fukui[4], K. Furusawa[4], J. B. Hearnshaw[6], Y. Itow[4], K. Kamiya[4], P. M. Kilmartin[7], A. Korpela[8], W. Lin[6], C. H. Ling[6], K. Masuda[4], Y. Matsubara[4], Y. Muraki[9], M. Nagaya[4], K. Ohnishi[10], T. Okumura[4], Y. C. Perrott[11], N. Rattenbury[12], To. Saito[13], T. Sako[4], S. Sato[14], L. Skuljan[2], D. J. Sullivan[8], T. Sumi[4], W. Sweatman[6], P. J. Tristram[7], P. C. M. Yock[11]
(The MOA Collaboration)
G. Bolt[15], G. W. Christie[16], D. L. DePoy[1], C. Han[17], J. Janczak[1], C.-U. Lee[18], F. Mallia[19], J. McCormick[20], B. Monard[21], A. Maury[19], T. Natusch[22], B.-G. Park[18], R. W. Pogge[1], R. Santallo[23], K. Z. Stanek[1]
(The μFUN Collaboration)
A. Udalski[24], M. Kubiak[24], M. K. Szymański[24], G. Pietrzyński[24,25], I. Soszyński[24], O. Szewczyk[24,25], Ł. Wyrzykowski[24,26], K. Ulaczyk[24]
(The OGLE Collaboration)
[1] Department of Astronomy, Ohio State University, 140 W. 18th Avenue, Columbus, OH 43210, USA; dong@astronomy.ohio-state.edu, gould@astronomy.ohio-state.edu, simkoz@astronomy.ohio-state.edu, gaudi@astronomy.ohio-state.edu, depoy@astronomy.ohio-state.edu, pogge@astronomy.ohio-state.edupogge, kstanek@astronomy.ohio-state.edu
[2] Institute of Information and Mathematical Sciences, Massey University, Private Bag 102-904, North Shore Mail Centre, Auckland, New Zealand; i.a.bond@massey.ac.nz
[3] Institute d'Astrophysique de Paris, 98bis Blvd Arago, Paris 75014, France
[4] Solar-Terrestrial Environment Laboratory, Nagoya University, Nagoya 464-8601, Japan
[5] Department of Physics, Notre Dame University, Notre Dame, IN 46556, USA; bennett@nd.edu
[6] University of Canterbury, Department of Physics and Astronomy, Private Bag 4800, Christchurch 8020, New Zealand
[7] Mt. John Observatory, P.O. Box 56, Lake Tekapo 8770, New Zealand
[8] School of Chemical & Physical Sciences, Victoria University, Wellington, P.O. Box 600, Wellington 6012, New Zealand; denis.sullivan@vuw.ac.nz
[9] Department of Physics, Konan University, Nishiokamoto 8-9-1, Kobe 658-8501, Japan
[10] Nagano National College of Technology, Nagano 381-8550, Japan
[11] Department of Physics, University of Auckland, Private Bag 92019, Auckland, New Zealand; yper006@ec.auckland.ac.nz, p.yock@auckland.ac.nz
[12] Jodrell Bank Centre for Astrophysics, The University of Manchester, Manchester, UK; njr@jb.man.ac.uk
[13] Tokyo Metropolitan College of Industrial Technology, Tokyo 116-0003, Japan
[14] Department of Physics and Astrophysics, Faculty of Science, Nagoya University, Nagoya 464-8602, Japan
[15] Center for Backyard Astrophysics, Perth, Australia; gbolt@iinet.net.au
[16] Auckland Observatory, Auckland, New Zealand; gwchristie@christie.org.nz
[17] Department of Physics, Institute for Basic Science Research, Chungbuk National University, Chongju 361-763, Korea; cheongho@astroph.chungbuk.ac.kr
[18] Korea Astronomy and Space Science Institute, Daejon 305-348, Korea; leecu@kasi.re.kr, bgpark@kasi.re.kr
[19] Campo Catino Austral Observatory, San Pedro de Atacama, Chile
[20] Farm Cove Observatory, Centre for Backyard Astrophysics, Pakuranga, Auckland, New Zealand; farmcoveobs@xtra.co.nz
[21] Bronberg Observatory, Pretoria, South Africa; lagmonar@nmisa.org
[22] Institute for Radiophysics and Space Research, AUT University, Auckland, New Zealand; tim.natusch@aut.ac.nz
[23] Southern Stars Observatory, Tahiti; obs930@southernstars-observatory.org
[24] Warsaw University Observatory, Al. Ujazdowskie 4, 00-478 Warszawa, Poland; udalski@astrouw.edu.pl, soszynsk@astrouw.edu.pl, msz@astrouw.edu.pl, mk@astrouw.edu.pl, pietrzyn@astrouw.edu.pl, szewczyk@astrouw.edu.pl, wyrzykow@astrouw.edu.pl, kulaczyk@astrouw.edu.pl
[25] Universidad de Concepción, Departamento de Fisica, Casilla 160-C, Concepción, Chile
[26] Institute of Astronomy Cambridge University, Madingley Road, CB3 0HA Cambridge, UK; wyrzykow@ast.cam.ac.uk
Received 2008 September 17; accepted 2009 April 17; published 2009 June 4

ABSTRACT

We report the detection of the cool, Jovian-mass planet MOA-2007-BLG-400Lb. The planet was detected in a high-magnification microlensing event (with peak magnification $A_{\rm max} = 628$) in which the primary lens transited the source, resulting in a dramatic smoothing of the peak of the event. The angular extent of the region of perturbation due to the planet is significantly smaller than the angular size of the source, and as a result the planetary signature is also smoothed out by the finite source size. Thus, the deviation from a single-lens fit is broad and relatively weak (approximately few percent). Nevertheless, we demonstrate that the planetary nature of the deviation can be unambiguously ascertained from the gross features of the residuals, and detailed analysis yields a fairly precise planet/star mass ratio of $q = (2.5^{+0.5}_{-0.3}) \times 10^{-3}$, in accord with the large significance ($\Delta\chi^2 = 1070$) of the detection. The planet/star projected separation is subject to a strong close/wide degeneracy, leading to two indistinguishable solutions that differ in separation by a factor of ~8.5. Upper limits on flux from the lens constrain its mass to be $M < 0.75\ M_\odot$ (assuming that it is a main-sequence star). A Bayesian analysis that includes all available observational constraints indicates a primary in the Galactic bulge with a mass of ~0.2–0.5 $M_\odot$ and thus a planet mass of ~0.5–1.3 $M_{\rm Jup}$. The separation and equilibrium temperature are

∼5.3–9.7 AU (∼0.6–1.1 AU) and ∼34 K (∼103 K) for the wide (close) solution. If the primary is a main-sequence star, follow-up observations would enable the detection of its light and so a measurement of its mass and distance.

Key words: Galaxy: bulge – gravitational lensing – planetary systems

Online-only material: color figures

1. INTRODUCTION

In the currently favored paradigm of planet formation, the location of the snow line in the protoplanetary disk plays a pivotal role. Beyond the snow line, ices can condense, and the surface density of solids is expected to be higher by a factor of several relative to its value just inside this line. As a result of this increased surface density, planet formation is expected to be most efficient just beyond the snow line, whereas for increasing distances from the central star the planet formation efficiency drops, as the surface density decreases and the dynamical time increases (Lissauer 1987). In this scenario, gas-giant planets must form in the region of the protoplanetary disk immediately beyond the snow line, as the higher surface density is required to build icy protoplanetary cores that are sufficiently massive to accrete a substantial gaseous envelope while there is remaining nebular gas (Pollack et al. 1996). Low-mass primaries are expected to be much less efficient at forming gas giants because of the longer dynamical times and lower surface densities at the snow lines of these stars (Laughlin et al. 2004; Ida & Lin 2005; Kennedy & Kenyon 2008). Migration due to nebular tides and other dynamical processes can then bring the icy cores or gas giants from their formation sites to orbits substantially interior to the snow line (Lin et al. 1996; Ward 1997; Rasio & Ford 1996).

The precise location of the snow line in protoplanetary disks is a matter of some debate (e.g., Lecar et al. 2006), and is even likely to evolve during the epoch of planet formation, particularly for low-mass stars (Kennedy et al. 2006; Kennedy & Kenyon 2008). The condensation temperature of water is ∼170 K, and a fiducial value for the location of the snow line in solar-mass stars motivated by observations in our solar system is ∼2.7 AU. This may scale linearly with the stellar mass M, since the stellar luminosity during the epoch of planet formation scales as $\sim M^2$ for stars with $M \lesssim M_\odot$ (Burrows et al. 1993, 1997). Whereas the radial velocity and especially transit methods are most sensitive to planets that are close to their parent star at distances well inside the snow line, the sensitivity of the microlensing method peaks at planetary separations near the Einstein ring radius of the primary lens (Mao & Paczynski 1991; Gould & Loeb 1992), which is $\sim 3.5\ \mathrm{AU}\ (M/M_\odot)^{1/2}$ for typical lens and source distances of 6 kpc and 8 kpc, respectively. This corresponds to a peak sensitivity at equilibrium temperatures of $T_{\rm eq} \sim 150\ \mathrm{K}\ (M/M_\odot)$ for a mass–luminosity relation of the form $L \propto M^5$, and distances relative to the snow line of $\sim 1.3\ (M/M_\odot)^{-1/2}$ if the location of the snow line at the epoch of planet formation scales as M. Thus, microlensing is currently the best method of probing planetary systems in the critical region just beyond the snow line (Gould & Loeb 1992).

Planetary perturbations in microlensing events come in two general classes. The majority of planetary perturbations are expected to occur when a planet directly perturbs one of the two images created by the primary lens, as the image sweeps by the planet during the microlensing event (Gould & Loeb 1992). Although these perturbations are more common, they are also unpredictable and can occur at any time during the event. Early microlensing planet searches focused on this class of perturbations, as it was the first to be identified and explored theoretically (Gould & Loeb 1992; Bennett & Rhie 1996; Gaudi & Gould 1997). The second class of planetary perturbations occurs in high-magnification events, in which the source becomes very closely aligned with the primary lens (Griest & Safizadeh 1998). In such events, the two primary-lens images become highly distorted and sweep along nearly the entirety of the Einstein ring (Liebes 1964). These sweeping images probe subtle distortions of the Einstein ring caused by nearby planets, which will give rise to perturbations within the full width at half-maximum of the event (Bond et al. 2002; Rattenbury et al. 2002). Although high-magnification events are rare and so contribute a minority of the planetary perturbations, they are individually more sensitive to planets because the images probe nearly the entire Einstein ring. Furthermore, since the perturbations are localized to the peak of the event which can be predicted beforehand, they can be monitored more efficiently with limited resources than the more common low-magnification events.

For these reasons, current microlensing planet searches tend to deliberately focus on high-magnification events. Thus, of the seven prior microlensing planets discovered to date (Bond et al. 2004; Udalski et al. 2005; Beaulieu et al. 2006; Gould et al. 2006; Gaudi et al. 2008; Bennett et al. 2008), five have been found in high-magnification events, with peak magnifications ranging from $A = 40$ to $A = 800$. However, despite the fact that this planet-search strategy has proven to be so successful, the properties of the planetary perturbations generated in high-magnification events are less well understood than those in low-magnification events.

Most of the studies of the properties of planetary perturbations in high-magnification events have focused on the properties of the caustics, the locus of points defining one or more closed curves, upon which the magnification of a point source is formally infinite. The morphology and extent of the region of significant perturbation by the planetary companion can be largely understood by the shape and size of these caustic curves. Planetary perturbations in high-magnification events are caused by a central caustic located near the position of the primary, and thus several authors have considered the size and shape of these central caustics as a function of the parameters of the planet (Griest & Safizadeh 1998; Dominik 1999; Chung et al. 2005). These and other authors have identified several potential degeneracies that complicate the unique interpretation of central caustic perturbations. The first to be identified is a degeneracy such that the caustic structure (and so light-curve morphology) of a planet with mass ratio $q \ll 1$ and projected separation in units of the Einstein ring d not too close to unity is essentially identical under the transformation $d \leftrightarrow d^{-1}$ (Griest & Safizadeh 1998). A second degeneracy arises from the fact

[27] Microlensing Follow Up Network (μFUN)
[28] Microlensing Observations for Astrophysics (MOA) Collaboration

that very close or very wide roughly equal-mass binaries also produce perturbations near the peak of the light curves. These give rise to perturbations that have the same gross observables as planetary perturbations.

The severity of these degeneracies depends on both the specific parameters of the planetary/binary companion, as well as on the data quality and coverage. Griest & Safizadeh (1998) and Chung et al. (2005) demonstrated that the $d \leftrightarrow d^{-1}$ degeneracy is less severe for more massive planets with separations closer to the Einstein ring ($d \sim 1$). Empirically, this degeneracy was broken at the $\Delta\chi^2 \sim 4$ level for the relatively large mass ratio planetary companion OGLE-2005-BLG-071Lb (Dong et al. 2009), for which the light curve was well sampled, but was essentially unresolved for the low-mass ratio planetary companion MOA-2007-BLG-192Lb (Bennett et al. 2008), for which the planetary perturbation was poorly sampled. For the planetary/equal-mass binary degeneracy, Han & Gaudi (2008) argued that, although the gross features of central caustic planetary perturbations can be reproduced by very close or very wide binary lenses, the morphologies differ in detail, and thus this degeneracy can be resolved with reasonable light-curve coverage and moderate photometric precision. Indeed for every well sampled high-magnification event containing a perturbation near the peak (and that is not in the Chang & Refsdal 1979 limits), this degeneracy has been resolved (Albrow et al. 2002; Gould et al. 2006; Dong et al. 2009). Even for the relatively poorly sampled light curve of MOA-2007-BLG-192Lb, an equal-mass binary model is ruled out at $\Delta\chi^2 \sim 120$ (Bennett et al. 2008), although in this case this is partially attributable to the exquisite photometric precision (<1%).

One complication with searching for planets in high-magnification events is that, the higher the magnification, the more likely it is that the primary lens will transit the source. When this happens, the peak of the event is suppressed and smoothed out, as the lens strongly magnifies only a small portion of the source. If the source is also larger than the region of significant perturbations due to a planetary companion (roughly the size of the central caustic), then the planetary deviations will also be smoothed out and suppressed (Griest & Safizadeh 1998; Han 2007). These finite-source effects have potential implications for both the detectability of central caustic perturbations, as well as the ability to uniquely determine the planetary parameters, and in particular resolve the two degeneracies discussed above. In practice, the caustic structures of all four high-magnification planetary events (containing five planets) were larger than the source. Hence, while there were detectable finite-source effects in all cases (which helped constrain the angular Einstein radius and so the physical lens parameters), the planetary perturbations were in all four cases quite noticeable. Thus, the effect of large sources on the detectability and interpretation of central caustic perturbations has not been explored in practice.

Theoretical studies of detectability of central caustic perturbations when considering finite-source effects have been performed by Griest & Safizadeh (1998), Chung et al. (2005), and Han (2007). These authors demonstrated that the qualitative nature of planetary perturbations from central caustics is dramatically different for sources that are larger than the caustic. In particular, the detailed structure of the point-source magnification pattern, which generally follows the shape of the caustic, is essentially erased or washed out. Rather, the perturbation structure is characterized by a roughly circular region of very low level, almost imperceptible deviation from the single-lens form that is roughly the size of the source and centered on the primary lens. This region is surrounded by an annular rim of larger deviations that has a width roughly equal to the width of the caustic (Griest & Safizadeh 1998; Chung et al. 2005). Finally, there are less pronounced deviations that extend to a few source radii. Planets are detectable even if their central caustics are quite a bit smaller than the source, provided that the χ^2 deviation is sufficiently high. (Often $\Delta\chi^2 > 60$ is adopted, although $\Delta\chi^2 > 150$ may be more realistic.) The magnitude of these perturbations decrease as the ratio between the source size and caustic size increases, making it difficult to detect very small planets for large sources (Chung et al. 2005; Han 2007).

Although central caustics may formally be detectable when the source is substantially larger than the caustic, it remains a significant question whether these very washed out caustics can be recognized in practice, and even if they can, whether they can be uniquely interpreted in terms of planetary parameters. Indeed, it is unknown whether a washed out central caustic due to a planet can actually be distinguished from one due to a binary companion. This question is especially important with regard to low-mass planets. The size of the central caustic scales as the product of the planet/star mass ratio and a definite function of planet–star separation. Hence, taken as a whole, smaller planets produce smaller caustics, meaning that events of higher magnification are required to detect them. These are just the events that are most likely to have their peaks washed out by finite-source effects.

Here, we analyze the first high-magnification event with a buried signature of a planet, in which the source size is larger than the central caustic of the planet. The caustic is indeed so washed out that the event appears unperturbed upon casual inspection. However, the residuals to a point-lens fit are clear and highly significant. We show that one can infer the planetary (as opposed to binary) nature of the perturbation from the general pattern of these residuals, and that a detailed analysis constrains the mass ratio of the planet quite well, but leaves the close/wide ($d \leftrightarrow d^{-1}$) degeneracy intact. Hence, at least in this case, the fact that the caustic is buried in the source does not significantly hinder one's ability to uncover the planet and measure its mass ratio.

2. OBSERVATIONS

MOA-2007-BLG-400 [$(\alpha, \delta)_{J2000.0} = (18^h09^m41\overset{s}{.}98, -29°13'26\overset{''}{.}95)$, $(l, b) = (2\overset{°}{.}38, -4\overset{°}{.}70)$] was announced as a probable microlensing event by the Microlensing Observations in Astrophysics (MOA) Collaboration on 2007 September 5 ($HJD' \equiv HJD - 2450000 = 4349.1$), about 5 days before peak. The source star proves to be a bulge subgiant and so is somewhat brighter than average, but the event timescale was relatively short ($t_E \sim 15$ days) and observations had been interrupted for 6 days by bad weather. Taken together, the two latter facts account for the relatively late alert. By coincidence, the triggering observations took place on the same night that another event, OGLE-2007-BLG-349 (aka MOA-2007-BLG-379), was peaking at extremely high magnification with an already obvious planetary anomaly. After focusing exclusively on the latter event for the first 5 hr of the night, MOA resumed its normal field rotation for the last 1.5 hr, which led to the discovery of MOA-2007-BLG-400.

The Microlensing Follow Up Network (μFUN) began observing this as a possible high-magnification event on September 7, but did not mobilize intensive observations until UT 08:55

September 10, just 15 hr before peak, following a high-mag alert issued by MOA a few minutes earlier. Even at that point, the predicted minimum peak magnification was only $A_{\rm max} > 90$, which would have enabled only modest sensitivity to planets. Nevertheless, all stops were pulled and it was observed as intensively as possible from seven observatories, μFUN CBA Perth (Australia) 0.25 m unfiltered, μFUN Bronberg (South Africa) 0.35 m unfiltered, μFUN SMARTS (CTIO, Chile) 1.3 m V, I, H, μFUN Campo Catino Austral (CAO, Chile) 0.50 m unfiltered, μFUN Farm Cove (New Zealand) 0.35 m unfiltered, μFUN Auckland (New Zealand) 0.4 m R, and μFUN Southern Stars (Tahiti) 0.28 m unfiltered.

The source star lies just outside one of the Optical Gravitational Lensing Experiment (OGLE) fields (as defined by their field templates) and for this reason was not recognized as a microlensing event by the OGLE Early Warning System. However, due to small variations in pointing, there are a total of 452 OGLE images containing this source. Only two of these are *significantly* magnified, 10 days and 9 days before peak. Hence, the OGLE data do not help constrain the light-curve parameters. However, they are useful to study of the baseline behavior of the source (see the Appendix).

Essentially all of the "action," both the peak of the event and the planetary anomalies, occurred during the μFUN SMARTS (Chile) observations at CTIO, $4354.47 < {\rm HJD}' < 4354.69$, using the ANDICAM optical/IR dual-channel camera, and μFUN CAO (Chile) observations $4354.50 < {\rm HJD}' < 4354.70$. Most (45) of the optical CTIO observations over the peak were carried out in I band, with a few (eight) taken in V in order to measure the $(V-I)$ color. Each of these was a 5 minute exposure, with approximately 1 minute readout time between exposures. During each optical exposure, there were five dithered H-band exposures, each of 50 s, almost equally spaced over the 6 minute cycle time. That is, $53 \times 5 = 265$ H-band observations in all. Unfortunately, the source became so bright as it transited the lens (i.e., when the planetary anomalies were the strongest), which 14 I-band images were affected by nonlinearities and saturation in the detector response. We exclude these 14 I-band data points from analysis. The H-band photometry are not affected by this problem, therefore, with higher time resolution and more continuous coverage than the I-band data, the H-band data provide most of the constraining power to the microlens model.

There were 84 CAO unfiltered observations taken during the peak night. Unfortunately, the peak of the event was severely saturated and the clock zero point is not securely known, therefore, these data are not used in the analysis. However, the exposures during the times of maximum deviation from a point lens (i.e., when the caustic was crossing the stellar limb) are not saturated, and these qualitatively confirm the interpretation from the more detailed CTIO data.

The μFUN CTIO and MOA data are used in the analysis since they provide essentially all the constraints to the microlens model. Data from other μFUN sites are checked for consistency with the final models, and they are found to be well fitted by the best-fit model. The MOA data were reduced using the standard MOA difference imaging analysis (DIA) pipeline. The μFUN CTIO data were reduced using DIA developed by Woźniak (2000). The H-band data are affected by intrapixel sensitivity variations at the 1% level. Fortunately, the dither pattern was repeated almost exactly over the night of the peak, so that these variations follow the five-element dither pattern quite well. We therefore treat the H-band data as five independent data sets,

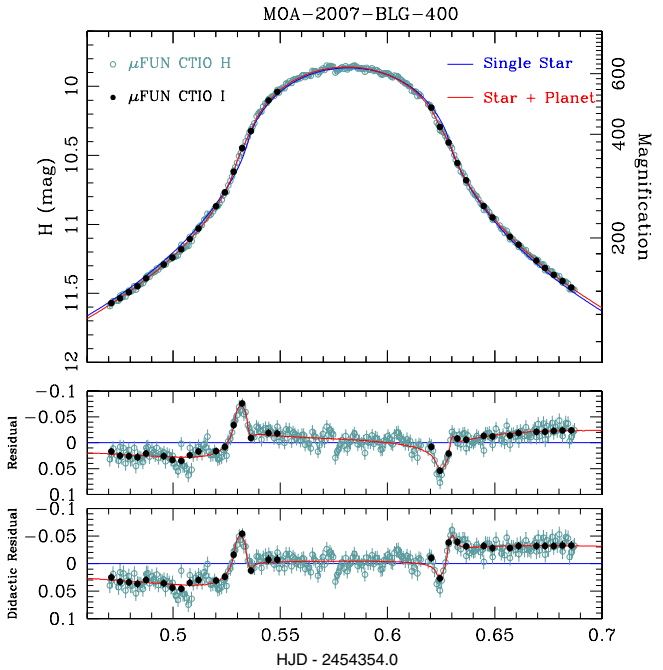

Figure 1. Top: light curve of MOA-2007-BLG-400 with data from μFUN CTIO (Chile) simultaneously taken in H (cyan), I (DIA, black). Models are shown for a point lens (blue) and planet–star system (red). There are five 50 s H exposures for each 300 s I (or V, not shown) exposure in 6 minutes cycles. Some I-band data at the peak suffer from saturation, and those points are therefore removed from the analysis (see the text). Middle: residuals for best-fit point-lens model and its difference with the planetary model. Note that in the top panel, the H data are shown as observed, while the I data are aligned. Normally, such alignment is straightforward because microlensing of point sources is achromatic. However, here there is significant chromaticity due to different limb darkening. The I-band points in the top panel are actually the residuals to the I-band limb-darkened model (middle panel), added to the H-band model curve (top panel). Bottom: residuals from a point-lens model with the same parameters as the planetary model, which can be directly compared with the "magnification map" in Figure 3. These "didactic residuals" are naturally more pronounced than those from the best-fit point lens.

which reduces χ^2 by 180 for 8 degrees of freedom. The H-band images show a triangular point-spread function (PSF), which is likely to introduce systematic errors into the photometry. As a cross-check, we also use the DIA package developed by Bond et al. (2001) to independently reduce these images.

3. MICROLENS MODEL

Despite the fact that the peak of MOA-2007-BLG-400 was "flattened" by finite-source effects, it nevertheless reached a very high peak magnification, $A_{\rm max} = 628$. However, even to the experienced eye, it looks like an ordinary point-lens light curve with pronounced finite-source effects. More detailed modeling is required to infer that it actually contains a Jovian mass-ratio planet.

Figure 1 shows the light curve together with the best-fit point-lens model (blue) and planetary model (red). Both include finite-source effects. The most pronounced features of the point-lens model residuals are a short positive spike on the rising side and a short negative spike on the falling side, each lasting about 30 minutes, which leave very similar traces in I and H. As displayed in Figure 2, these features clearly stand out in the reductions using both the Wozniak (top panel) and Bond (bottom panel) DIA packages. Each package introduces its own systematic deviations, but there are no obvious trends besides the above features that are supported by both reductions. These

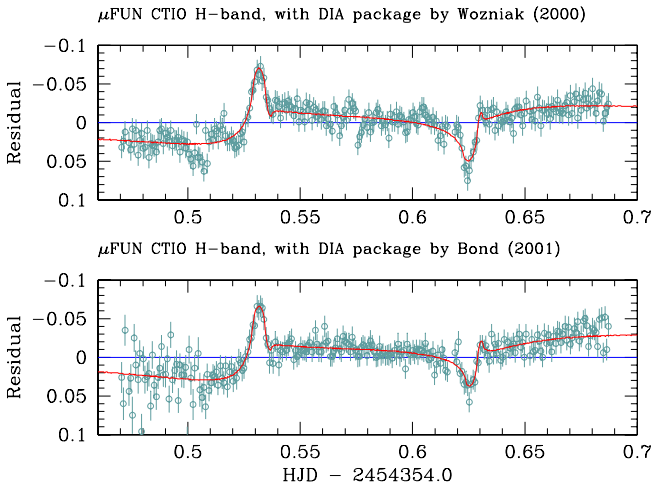

Figure 2. Comparisons of residuals to the best-fit point-lens models between two photometric reductions of μFUN H-band data, using the DIA packages developed by Woźniak (2000; top) and Bond et al. (2001; bottom). The red curve in each panel represents the difference of the best-fit planetary and point-lens models for that panel's reduction. Both reductions agree on the main planetary features, but each package introduces its own systematics. For example, the systematic deviations from the planetary model at HJD $\sim$ 2454354.57 shown in the top panel are not supported by the reductions of the Bond's package. During 2454354.46 $<$ HJD $<$ 2454354.51, most images have low transparency ($\lesssim$50%), which causes relatively large scatter in Bond's DIA reductions. In comparison, the reduction by Wozniak's DIA has smaller scatter during this period. However, the data exhibit some low-level systematics, which are not supported by the other reduction.

occur very close to the times that the point lens begins and ends its transit of the source (within the framework of this model). The timing of these deviations strongly suggests that they are due to microlensing rather than stellar variability. There are then two possible explanations: either the source is actually being transited by a more complicated caustic than a point lens (due to a binary or planetary companion) or the limb of the source is not being properly modeled. However, if one assumes a circular source, the latter explanation would imply symmetric residuals, whereas the actual residuals are closer to being antisymmetric. (We address the possibility of an elliptical source in the Appendix.) Indeed, this approximate antisymmetry extends to the less pronounced residual features, including the sustained deficit prior to the first spike (and sustained excess following the second one) as well as the declining residuals between the two spikes. The similarity of the I and H residuals in itself argues that the deviations are due to microlensing rather than some sort of stellar variability, which would not generally be expected to be achromatic.

The short durations of the spikes tell us that the central caustic is quite small, with "caustic width" $w \sim 30$ minutes/15 days $= 1.4 \times 10^{-3}$. This implies that the companion either has low-mass ratio, or is a very wide or very close binary companion. Formally, w is given by Equation (12) of Chung et al. (2005) as a very good approximation to the "short diameter" or "width" of a central caustic (see Figure 3). However, here the estimate is quite inexact not only because the width of the spikes is not precisely defined, but also because we do not know, at this point, the exact orientation of the caustic.

After some algebra, one finds that in two limiting regimes, the Chung et al. (2005) formula takes the forms,

$$w(d,q) \rightarrow \frac{4q}{d^2} \quad (d \gg 1), \qquad w(d,q) \rightarrow 4qd^2 \quad (d \ll 1) \tag{1}$$

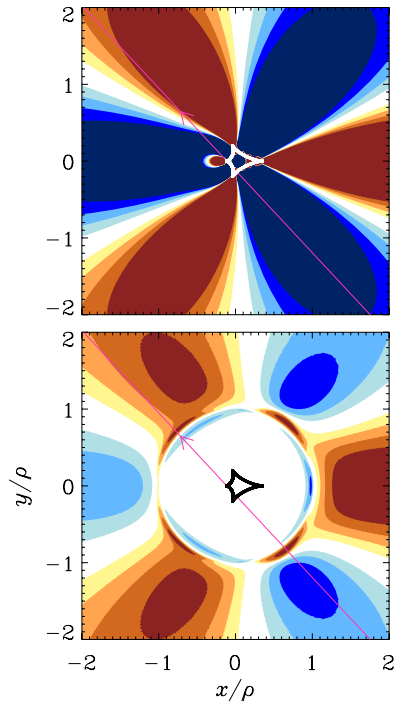

Figure 3. Magnification differences between of best-fit planetary model ($(q, d) = (0.0025, 2.9)$ and $(q, d) = (0.0026, 0.34)$ being nearly identical) and single-lens models, in units of the measured source size, $\rho = 0.0033$ Einstein radii. Contours show 1%, 2%, 3%, and 4%, deviations in the positive (brown) and negative (blue) directions. Top panel: single-lens geometry (t_0, u_0, t_E) is taken to be the same as in the planetary model, with no finite-source effects. Caustic (contour of infinite magnification) is shown in white. The deviations are very pronounced. Bottom panel: same as top panel, but including finite-source effects, which now explain the main features of the light curve. The trajectory begins with a negative deviation, then hits a narrow "brown ridge" causing the spike seen in the bottom panel of Figure 1, as the edge of the source first hits the caustic. Then there are essentially no deviations (white) while the source covers the caustic. The caustic exit induces a narrow "blue ridge" corresponding to the negative-deviation spike seen in Figure 1. Finally, the source runs along the long "brown ridge" corresponding to the prolonged postpeak mild excess seen in Figure 1.

and

$$w(d,q) \rightarrow \sqrt{\frac{27}{16}}\,\frac{q}{|d-1|} \qquad (d \sim 1), \tag{2}$$

where q is the companion/primary mass ratio and d is the separation in units of the Einstein ring. Note that in the first limit (Equation (1)), $w \rightarrow 4\gamma$, where γ is the shear. The crossover point for these approximations is $d = 2.3$ (or $d = 0.43$), at which point each is in error by about 15%. (For simplicity, we restrict the discussion here to the case $d > 1$. There is a well known $d \leftrightarrow d^{-1}$ degeneracy between the $d \ll 1$ and $d \gg 1$ limits, as can be guessed from the forms for w in Equation (1). This degeneracy will prove to be almost perfect in this case, see Section 3.3). Hence, in the first limit, $d \sim 50q^{1/2}$, implying that if q were in the "binary range" ($|\log q| < 1$), then d would be quite large. That is, the central caustic would be generated by a nearly pure shear and therefore would have a nearly symmetric, diamond-shaped, Chang & Refsdal (1979) form. In the point-lens model, the lens passes almost directly over the center of the source. For this trajectory, a symmetric caustic would yield symmetric residuals, in sharp contrast to Figure 1. On the other hand, for the opposite limit, $q \sim 1 \times 10^{-3}(d-1)$, which lies squarely in the planetary regime. Thus, simple arguments already argue strongly in favor of a planetary companion that is fairly near the Einstein ring.

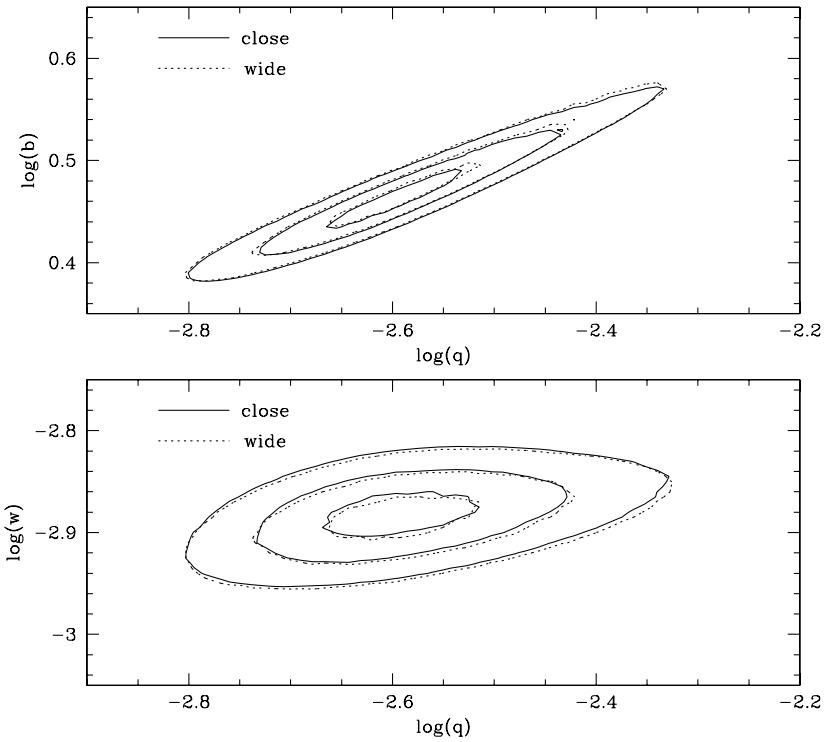

Figure 4. Contours of $\Delta\chi^2 = 1,\ 4,\ 9$ relative to the minimum as a function of planet–star mass ratio q and projected planet–star separation d (top), as well as "short caustic diameter" (see Figure 3) w (bottom). w (in units of $\theta_{\rm E}$) is a function of q and d (see the text). The solution shown here corresponds to $q = (2.5^{+0.5}_{-0.3}) \times 10^{-3}$ and $d = 2.9 \pm 0.2$ (or $d = 0.34^{+0.03}_{-0.02}$). These values of d correspond to physical separations and equilibrium temperatures of ∼5.3–9.7 AU, ∼34 K and ∼0.6–1.1 AU, ∼103 K for the close and wide solutions, respectively.

3.1. Hybrid Pixel/Ray Map Algorithm

Notwithstanding these arguments, we conduct a massive blind search for companions over a very broad range of masses using a modified version of the "magnification map" technique of Dong et al. (2006), which was specifically designed for high-magnification events. The original approach was, for each given $(d,\ q)$ pair, to shoot rays over a fairly narrow annulus (say, 0.01 Einstein radii) around the Einstein ring in the image plane and to sort these rays in pixels on the source plane. Then for each source position being modeled (i.e., each data point), one would identify the pixels that intersected the source and would check each ray contained in these pixels to determine whether it landed on the source and, if so, evaluate the source surface brightness at that position. In the initial broad search, three parameters $(d,\ q,\ \alpha)$ are held fixed on a grid of values, while the remaining parameters ($t_0,\ u_0,\ t_{\rm E},\ \rho$, and possibly others) are varied to minimize χ^2 at each grid point. Here, α is the angle of the source trajectory relative to the binary axis, t_0 is the time of closest approach to the adopted center of the lens geometry (usually the center of mass), u_0 is the source-lens separation at this time in units of the Einstein radius, ρ is the source radius in the same units, and $t_{\rm E}$ is the Einstein crossing time. This division is efficient because (1) $(t_0,\ u_0,\ t_{\rm E},\ \rho)$ are usually approximately known from the general structure of the light curve, so minimization over these parameters is straightforward once $(d,\ q,\ \alpha)$ are fixed and (2) $(d,\ q)$ define the map, which naturally facilitates minimization of other parameters except for α, whose value is not usually even approximately obvious from the light curve.

The new approach differs principally in that the pixels that are contained entirely within the source are now evaluated as a whole, i.e., by the total number of rays in that pixel. Pixels that cross the source boundary are still evaluated ray-by-ray, as previously. This primary change then leads to several other changes. First, for each pixel, we record not only the geometric center but also the centroid of the rays. The surface brightness is then evaluated at the latter position. Second, the pixels are made much smaller, to minimize both the number of rays that must be evaluated individually and the surface-brightness variations across the pixel (which are corrected only to first order by the ray-centroid scheme just mentioned). Typically, there are a few hundreds of pixels per source. Third, the pixels are hexagonal, since this is the most compact tiling possible, i.e., the closest tile shape to a circle. Fourth, the source positions outside the map region are evaluated using the hexadecapole and quadrupole approximation of Gould (2008; see also Pejcha & Heyrovský 2009). Finally, we use Markov chain Monte Carlo (MCMC) for the χ^2 minimization.

3.2. The (w, q) Grid of Lens Geometries

The initial search for solutions is conducted over a rectilinear grid in (w, q) rather (d, q). Since the short diameter, or "caustic width," w, is a monotonic function of the star–planet separation d (at fixed planet/star mass ratio q), these formulations are in some sense equivalent. However, for many events (including the present one) the short diameter w can be estimated by simple examination of the data. In these cases, the search space is both more regular and easier to define in terms of the (w, q) grid. In particular, Equation (2) shows that at fixed w, d moves very close to 1 for very low q.

3.3. Best-fit Model

We consider short diameters w over the range $-3.5 \leqslant \log w \leqslant -2$ and companion mass ratios $-4 \leqslant \log q \leqslant 0$,

focusing on the regime $d \geqslant 1$. We find that there is only one local minimum in this range. The range of allowed solutions is well localized around this minimum, with

$$q = \left(2.5^{+0.5}_{-0.3}\right) \times 10^{-3}, \quad d = 2.9 \pm 0.2,$$
$$w = (1.30 \pm 0.06) \times 10^{-3}, \tag{3}$$

with the last quantity being, of course, dependent on the first two. Figure 4 shows the $\Delta\chi^2 = 1$, 4, 9 contours with respect to the mass ratio q and the projected planet–star separation d along with the short diameter w. The main point to note is that these parameters are quite well constrained. Note that, as expected, d and q are strongly correlated, while w and q are basically uncorrelated. We also perform similar searches using the alternative H-band reduction by Bond's DIA package. The solutions agree with the above to well within 1σ, but the parameters have larger uncertainties: $q = (2.6 \pm 0.7) \times 10^{-3}$, $d = 2.9 \pm 0.3$, and $w = (1.26 \pm 0.09) \times 10^{-3}$. We therefore adopt results from the Wozniak-based reductions, noting that they may subject to systematic errors $\lesssim 1\sigma$.

Figure 3 shows the source trajectory and the central caustics as well as the differences in magnification between the best-fit planetary model and its corresponding single-lens model. This geometry nicely accounts for the main features of the point-lens residuals seen in Figure 1. The regions beyond the "back walls" (long segments) of the caustic are somewhat demagnified, which accounts for the initial depression of the light curve. As the source crosses the "back wall" of the caustic, it spikes. After the source has exited the caustic, it continues to suffer additional magnification due to the "ridge" of magnification that extends from the trailing cusp.

We also conducted a similar blind search as above, but concentrating on the regime $d < 1$. As expected, we recover the well-known $d \leftrightarrow d^{-1}$ degeneracy, and find a solution with essentially the same mass ratio $q = (2.6 \pm 0.4) \times 10^{-3}$, but with $d = 2.9^{-1} = 0.34^{+0.03}_{-0.02}$, and the wide solution is slightly preferred by $\Delta\chi^2 = 0.2$ (see Table 1). Thus, although each solution is well localized to its respective minimum, this discrete degeneracy implies that the projected separation can take on two values that differ by a factor of ~8.5. The severity of the degeneracy can be traced to the planetary parameters. Although the planet/star mass ratio is quite large, which tends to reduce the severity of the degeneracy, the planet lies quite far from the Einstein ring, which tends to make it more severe. Actually, a better measure of the overall expected asymmetry between the d and d^{-1} solutions is the short diameter w, which in this case is small, implying a severe degeneracy. Indeed, the caustic structure and magnification pattern of the two solutions are nearly identical. In this case, the large size of the source has competing influences on the ability to resolve the degeneracy. On one hand, the large size of the source serves to suppress the planetary deviations, thus making subtle differences more difficult to distinguish. On the other hand, the large source implies that a large fraction of the planetary perturbation region is probed. In this case, the source probes essentially the entire region of significant planetary perturbation, as can be seen in Figure 3. This is important for distinguishing between the solutions, as the largest difference between the magnification patterns of the two degenerate solutions occurs in the region near the tip of the arrow-shaped caustic (Griest & Safizadeh 1998). From Figure 3, it is clear that this region would have been entirely missed if the source had been substantially smaller than the caustic.

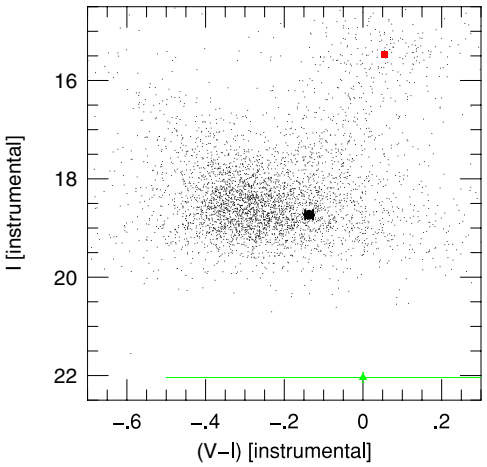

Figure 5. Instrumental color–magnitude diagram of field containing MOA-2007-BLG-400. The color and magnitude of the source (filled circle) are derived from the fit to the light curve, which also yields an upper limit for the I-band blended flux (triangle). The large error bar on the latter point indicates a complete lack of information about its V-band flux. The clump centroid is indicated in square. From the source-clump offset, we estimate $[I, (V-I)]_{0,s} = (17.57, 0.81)$, implying it has angular radius $\theta_* = 1.05$ μas. Assuming that the source lies at 8 kpc, it has $[M_I, (V-I)]_{0,s} = (3.07, 0.81)$, making it a subgiant. The lack of blended light allows us to place an upper limit on the lens flux, which implies that it has mass $M < 0.75\ M_\odot$. See the text.

(A color version of this figure is available in the online journal.)

4. FINITE-SOURCE EFFECTS

In addition to (d, q), the model also yields the source radius relative to the Einstein radius,

$$\rho = \theta_*/\theta_{\rm E} = (3.29 \pm 0.08) \times 10^{-3}. \tag{4}$$

We then follow the standard (Yoo et al. 2004) technique to determine the angular source radius,

$$\theta_* = 1.05 \pm 0.05\ \mu{\rm as}. \tag{5}$$

That is, we first adopt $[(V-I)_0, I_0]_{\rm clump} = (1.00, 14.32)$ for the dereddened position of the clump. We then measure the offset of the source relative to the clump centroid $\Delta[(V-I), I] = (-0.19, 3.25)$, to obtain $[(V-I)_0, I_0]_s = (0.81, 17.57)$ (see Figure 5). The instrumental source color is derived from model-independent regression of the V and I flux, while the instrumental magnitude is obtained from the light-curve model. We convert $(V-I)$ to $(V-K)$ using the color–color relations of Bessell & Brett (1988), yielding $(V-K)_0 = 1.75$, and then obtain Equation (5) using the color/surface-brightness relations of Kervella et al. (2004). Combining Equations (4) and (5) give $\theta_{\rm E} = \theta_*/\rho = 0.32$ mas. And combining this with the definition $\theta_{\rm E}^2 = \kappa M \pi_{\rm rel}$, where M is the lens mass, $\pi_{\rm rel}$ is the source-lens relative parallax, and $\kappa = 4G/c^2{\rm AU} \sim 8.1$ mas $M_\odot^{-1}$, together with the measured Einstein timescale, $t_{\rm E} = 14.3 \pm 0.3$ days, we obtain

$$M = 0.10\ M_\odot \left(\frac{\pi_{\rm rel}}{125\ \mu{\rm as}}\right)^{-1} \tag{6}$$

and

$$\mu_{\rm rel} = \frac{\theta_{\rm E}}{t_{\rm E}} = 8\ {\rm mas\ yr}^{-1}. \tag{7}$$

The relatively high lens-source relative proper motion $\mu_{\rm rel}$ is mildly suggestive of a foreground disk lens, but still quite

consistent with a bulge lens. Since $\pi_{\rm rel} = 125\ \mu$as corresponds to a lens distance $D_L = 4$ kpc (assuming source distance $D_S = 8$ kpc), Equation (6) implies that if the lens did lie in the foreground, then it would be a very low mass star or a brown dwarf.

Assuming that the source lies at a Galactocentric distance modulus 14.52, its dereddened color and magnitude imply that $[(V-I)_0, M_I] = (0.81, 3.07)$, making it a subgiant.

5. LIMB DARKENING

As illustrated in Figure 1, the principal deviations from a point-lens light curve occur at the limb of the star. This prompts us to investigate the degree to which the planetary solution is influenced by our treatment of limb darkening. The results that we report are based on a fit to the H-band surface-brightness profile of the form

$$\frac{S(\vartheta)}{\bar{S}_\lambda} = 1 - \Gamma\left(1 - \frac{3}{2}\cos\vartheta\right) - \Lambda\left(1 - \frac{5}{4}\cos^{1/2}\vartheta\right), \quad (8)$$

where Γ and Λ are the linear and square root parameters, respectively, and where ϑ is the angle between the normal to the stellar surface and the line of sight, i.e., $\sin\vartheta = \theta/\theta_*$. See An et al. (2002) for the relation between (Γ, Λ) and the usual (c, d) formalism.

In deriving the reported results, we fix the H-band limb-darkening parameters $(\Gamma, \Lambda) = (-0.15, 0.69)$, corresponding to $(c, d) = (-0.21, 0.79)$ from Claret (2000) for a star with effective temperature $T_{\rm eff} = 5325$ K and $\log g = 4.0$. These stellar parameters are suggested by comparison to Yale–Yonsei isochrones (Demarque et al. 2004) for the dereddened color and absolute magnitude reported in Section 4. We also perform fits in which Γ and Λ are allowed to be completely free. From these fits, we find that our best-fit model has $(\Gamma, \Lambda) = (-0.64, 1.47)$. Γ and Λ are highly correlated, so their individual values are not of interest, and the surface-brightness profiles generated by these two sets of (Γ, Λ) are qualitatively similar. In the present context, however, the key point is that when we fix the limb-darkening parameters at the Claret (2000) values, the contours in Figure 4 remain essentially identical and the best-fit values change by much less than 1σ.

Because of lower point density and the aforementioned problems with the I data over the peak, we only attempt a linear limb-darkening fit, i.e., we use Equation (8) with $\Lambda \equiv 0$, and we adopt $\Gamma = 0.47$ from Claret (2000).

6. BLENDED LIGHT

In the crowded fields of the Galactic bulge, the photometered light of a microlensing event rarely comes solely from the lensed source. Rather there is typically additional light that is blended with the source but is not being lensed. This light can arise from unrelated stars that happen to be projected close enough to the line of sight to be blended with the source, or it can come from companions to the source, companions to the lens, or the lens itself. This last possibility is most interesting because, if the lens flux can be isolated and measured, it provides strong constraints on the lens properties, and in this case would enable a complete solution of the lens mass and distance, when combined with the measurement of $\theta_{\rm E}$ (e.g., Bennett et al. 2007).

To investigate the blended light, we begin by using the method of Gould & An (2002) to construct an image of the field with the source (but not the blended light) removed, and compare this to a baseline image, which of course contains both the source and the blended light (see Figure 6). In these images, the source/blend is immersed in the wings of a bright star (roughly 3.7 mag brighter than the source), which lies about 2″ away. On the baseline image, the source/blend is noticeable against this background, but hardly distinct. On the source-subtracted image, the blend is not directly discernible.

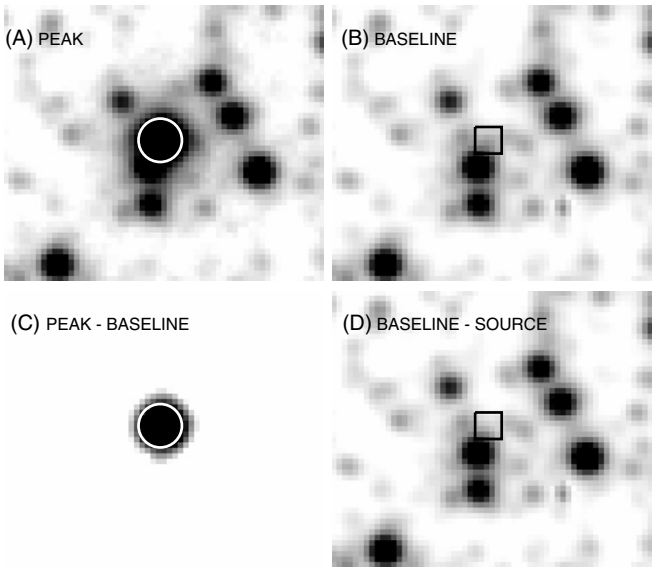

Figure 6. Constraining the blended flux from CTIO I-band images. A good-seeing baseline image B (upper right) is subtracted from an image taken at magnification 245 (A, upper left), and the resulting image C is shown in the bottom left panel. The white circles on images A and C indicate the source positions. Then C is scaled by 1/244 in flux and subtracted from image B to generate image D, which has the source contribution removed from the baseline image. As described in the text, we fit PSF to the stars close to the source, and subtract them from images B and D. After subtraction, the flux sums in a 1.″8 square (shown as black boxes on right two panels) are 564 ADU and −28 ADU, respectively. Nondetection of the blend constrains the blend-source flux ratio to be less than 5%.

To make a quantitative estimate of the blend flux, we fit the region in the immediate vicinity of the bright star to the form $F = a_1 + a_2 \times$ PSF, where "PSF" is the point-spread function determined from the DIA analysis. We then subtract the best-fit flux profile from the image. This leaves a clear residual at the position of the source/blend in the baseline image, but just noise in the source-subtracted image. We add all the flux in a 1.″8 square centered on the lens, finding 564 ADU and −28 ADU, respectively. We conclude that the I-band flux blend/source ratio is $f_b/f_s < 0.05$. Of course, even if we had detected blended light, it would be impossible to tell whether it was directly coincident with the source. If it were, this would imply that this light would be directly associated with the event, i.e., being either the lens itself or a companion to the lens or the source. Hence, this measurement is an upper limit on the light from the lens in two senses: no light is definitively measured, and if it were we do not know that it came from the lens. Combining this limit with Equation (6), and assuming that the lens is a main-sequence star, it must then be less massive than $M < 0.75\ M_\odot$, and so must have relative parallax $\pi_{\rm rel} > 15$ mas. This implies a lens–source separation $D_S - D_L > 1$ kpc, which certainly does not exclude bulge lenses. Indeed, if the lens were a K dwarf in the Galactic bulge, it would saturate this limit.

7. DISCUSSION

MOA-2007-BLG-400 is the first high-magnification microlensing event for which the central caustic generated by a planetary companion to the lens is completely enveloped by the source. As a comparison, the planetary caustic of OGLE-2005-BLG-390 (Beaulieu et al. 2006) is smaller than its clump-giant source star in angular size. When the planetary caustics is covered by the source, the finite-source effects broaden the "classic" Gould & Loeb (1992) planetary perturbation features (Gaudi & Gould 1997). By contrast, planet-induced deviations in MOA-2007-BLG-400 are mostly obliterated, rather than being broadened, because the source crosses the central caustic rather than the planetary caustic. We showed, nevertheless, that the planetary character of the event can be inferred directly from the light-curve features and that the standard microlensing planetary parameters $(d, q) = (2.9, 2.5 \times 10^{-3})$ can be measured with good precision, up to the standard close/wide $d \leftrightarrow d^{-1}$ degeneracy. We demonstrated that, in this case, the close/wide degeneracy is quite severe, and the wide solution is only preferred by $\Delta\chi^2 = 0.2$. This is unfortunate, since the separations of the two solutions differ by a factor of $\sim$8.5. We argued that the severity of this degeneracy was primarily related to the intrinsic parameters of the planet, rather than being primarily a result of the large source size.

Although the mass ratio alone is of considerable interest for planet formation theories, one would also like to be able to translate the standard microlensing parameters to physical parameters, i.e., the planet mass $m_p = qM$, and planet–star projected separation $r_\perp = d\theta_{\rm E} D_L$. Clearly, this requires measuring the lens mass M and distance D_L. In this case, the pronounced finite-source effects have already permitted a measurement of the Einstein radius $\theta_{\rm E} = 0.32$ mas, which gives a relation between the mass and lens-source relative parallax (Equation (6)). This essentially yields a relation between the lens mass and distance, since the source distance is close enough to the Galactic center that knowing D_L is equivalent to knowing $\pi_{\rm rel}$. Therefore, a complete solution could be determined by measuring either M or D_L, or some combination of the two.

One way to obtain an independent relation between the lens mass and distance is to measure the microlens parallax, $\pi_{\rm E}$. There are two potential ways of measuring $\pi_{\rm E}$. First, one can measure distortions in the light curve arising from the acceleration of the Earth as it moves along its orbit. Unfortunately, this is out of the question in this case because the event is so short that these distortions are immeasurably small. Second, one can measure the effects of terrestrial parallax, which gives rise to differences between the light curves simultaneously observed from two or more observatories separated by a significant fraction of the diameter of the Earth. Practically, measuring these differences requires a high-magnification event, which would appear to make this event quite promising. Unfortunately, although we obtained simultaneous observations from two observatories separated by several hundred kilometers during the peak of the event, one of these data sets suffers from large systematic errors and an unknown time zero point, rendering it unusable for this purpose.

The only available alternative for breaking the degeneracy between the lens mass and distance would be to measure the lens flux, either under the glare of the source or, at a later date, to separately resolve it after it has moved away from the line of sight to the source (Alcock et al. 2001; Kozłowski et al. 2007). Panels (e) and (f) of Figure 7 show the Bayesian estimates of the lens brightness in I band and H band, respectively. If the lens flux is at least 2% of the source flux, then the former kind of measurement could be obtained from a single epoch *Hubble Space Telescope* (*HST*) observation, provided it were carried out in the reasonably near future. At roughly 99% probability, the blended light would be either perfectly aligned with the source (and so associated with the event) or well separated from it. *HST* images can be photometrically aligned to the ground-based images using comparison stars with an accuracy of better than 1%. Hence, photometry of the source+blend would detect the blend, unless it were at least 4 mag fainter than the source. In principle, the blend could be a companion to either the source or lens. Various arguments can be used to constrain either of those scenarios. We do not explore those here, but see Dong et al. (2009). If the lens is not detectable by current epoch *HST* observations (or no *HST* observations are taken), then it will be detectable by ground-based AO H-band observations in about five years. This is because the lens–source relative proper motion is measured to be $\mu_{\rm rel} = 8$ mas yr^{-1}, and the diffraction limit at H band on a 10 m telescope is roughly 35 mas. If the lens proves to be extremely faint, then a wider separation (and hence a few years more time baseline) would be required.

In the absence of additional observational constraints, we must rely on a Bayesian analysis to estimate the properties of the host star and planet, which incorporates priors on the distribution of lens masses, distances, and velocities (Dominik 2006; Dong et al. 2006). This is a standard procedure, which we only briefly summarize here. We adopt a Han & Gould (1995) model for the Galactic bar, a double-exponential disk with a scale height of 325 pc, and a scale length of 3.5 kpc, as well as other Galactic model parameters as described in Bennett & Rhie (2002). We incorporate constraints from our measurement of the lens angular Einstein radius $\theta_{\rm E}$ and the event timescale, as well as limits on the microlens parallax and I-band magnitude of the lens. In practice, only the measurements of $\theta_{\rm E}$ and $t_{\rm E}$ provide interesting constraints on these distributions. In addition, we include the small penalty on the close solution, $\exp(-\Delta\chi^2/2)$, where the wide solution is favored by $\Delta\chi^2 = 0.2$. For the estimates of the planet semimajor axis, we assume circular orbits and that the orbital phases and cos(inclinations) are randomly distributed.

The resulting probability densities for the physical properties of the host star, as well as selected properties of the planet, are shown in Figure 7. The Bayesian analysis suggests a host star of mass $M = 0.30^{+0.19}_{-0.12}\ M_\odot$ at distance of $D_L = 5.8^{+0.6}_{-0.8}$ kpc. In other words, given the available constraints, the host is most likely an M dwarf, probably in the foreground Galactic bulge. Given that the planet/star mass ratio is measured quite precisely, the probability distribution for the planet mass is essentially just a rescaled version of the probability distribution for the host star mass. We find $m_p = 0.83^{+0.49}_{-0.31}\ M_{\rm Jup}$. The close/wide degeneracy is apparent in the probability distribution for the semimajor axis a. We estimate $a_{\rm close} = 0.72^{+0.38}_{-0.16}$ AU for the close solution, and $a_{\rm wide} = 6.5^{+3.2}_{-1.2}$ AU for the wide solution. The equilibrium temperatures for these orbits are $T_{\rm eq.,close} = 103^{+28}_{-26}$ K and $T_{\rm eq.,wide} = 34 \pm 9$ K for the close and wide solutions, respectively.

Thus, our Bayesian analysis suggests that this system is mostly likely a bulge mid-M dwarf, with a Jovian-mass planetary companion. The semimajor axis of the planetary companion is poorly constrained primarily because of the close/wide degeneracy, but the implied equilibrium temperatures are cooler

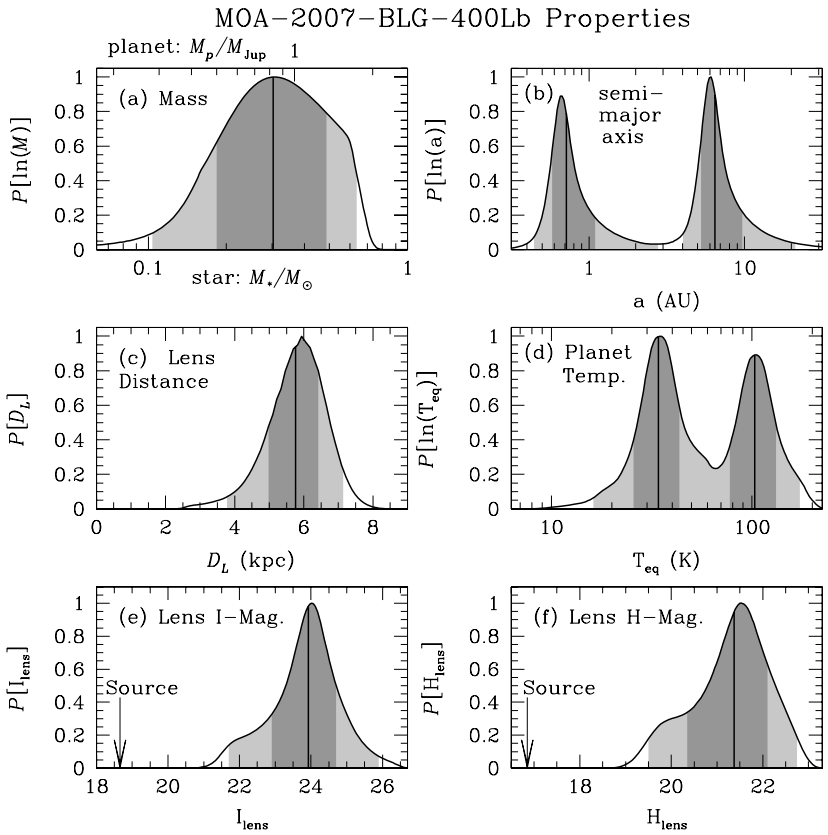

Figure 7. Bayesian relative probability densities for the physical properties of the planet MOA-2007-BLG-400Lb and its host star. (a) Mass of the host star. (b) Planet semimajor axis. (c) Distance to the planet/star system. (d) Equilibrium temperature of the planet. (e) *I*-band magnitude of the host star. (f) *H*-band magnitude of the host star. In panel (a), we also show the probability density for the planet mass, which is essentially a rescaling of that of the host star, because the mass ratio is measured so precisely $q = (2.5^{+0.5}_{-0.3}) \times 10^{-3}$. In all panels, the solid vertical lines show the medians, and the 68.3% and 95.4% confidence intervals are enclosed in the dark and light shaded regions, respectively. In panels (b) and (d), the probability distributions for wide and close degenerate solutions are computed separately, and then the close solution is weighted by $\exp(-\Delta\chi^2/2)$, where $\Delta\chi^2 = 0.2$ is the difference between them. These distributions are derived assuming priors obtained from standard models of the mass, velocity, and density distributions of stars in the Galactic bulge and disk, and include constraints from the measurements of lens angular Einstein radius θ_E and the timescale of the event t_E, as well as limits on the *I*-band magnitude of the lens. In practice, only the measurements of θ_E and t_E provide interesting constraints on these distributions.

Table 1
Best-fit Planetary Models

Model[a]	$t_0 - t_{ref}$[b] (day)	u_0	t_E (day)	d	q	α[c] (deg)	ρ
Close	0.08107	0.00025	14.41	0.34	0.0026	227.06	0.00326
Wide	0.08106	0.00027	14.33	2.87	0.0025	226.99	0.00329

Notes.

[a] The wide solution is preferred over best-fit single-lens model by $\Delta\chi^2 = 1070.04$ and the close solution by $\Delta\chi^2 = 1069.84$.

[b] t_{ref} = HJD 2454354.5 (2007 September 11, 00:00 UT).

[c] The geometry of the source trajectory is visualized in Figure 3, in which the planet is to the right of the lens star. t_0, u_0, and α are defined with respect to the "center of magnification," which is the center of mass of the star/planet system for the close model and $q/(1+q)/d$ away from the position of the lens star toward the direction of the planet for the wide model.

than the condensation temperature of water. Specifically, we find that $T_{eq} \lesssim 173$ K at 2σ level. Alternatively, if we assume that the snow line is given by $a_{snow} = 2.7\ \mathrm{AU}\,(M/M_\odot)$, we find for this system a snow line distance of ~0.84 AU, essentially the same as the inferred semimajor axis of the close solution. Thus, this planet is quite likely to be located close to or beyond the snow line of the system.

Although we cannot distinguish between the close and wide solutions for the planet separation, theoretical prejudice in the context of the core-accretion scenario would suggest that a gas-giant planet would be more likely to form just outside the snow line, thus preferring the close solution. However, we have essentially no observational constraints on the frequency and distribution of Jupiter-mass planets at the separations implied by the wide solution (~5.3–9.7 AU), for such low-mass primaries. Unfortunately, the prospects for empirically resolving the close/wide degeneracy in the future are poor. The only possible method of doing this would be to measure the radial velocity signature of the planet. Given the faintness of the host star (see Section 6 and Figure 7), this will likely be impossible with current or near-future technology.

The mere existence of a gas-giant planet orbiting a mid-M dwarf is largely unexpected in the core-accretion scenario, as formation of such planets is thought to be inhibited in such low-mass primaries (Laughlin et al. 2004). Observationally, however, although the frequency of Jovian companions to M dwarfs with $a \lesssim 3$ AU does appear to be smaller than the corresponding frequency of such companions to FGK dwarfs (Endl et al. 2006; Johnson et al. 2007; Cumming et al. 2008), several Jovian-mass companions to M dwarfs are known (see Dong et al. 2009 for a discussion), so this system would not be unprecedented. Furthermore, it must be kept in mind that the estimates of stellar (and so planet) mass depend on the validity of the priors, and even in this context have considerable uncertainties.

Most of the ambiguities in the interpretation of this event would be removed with a measurement of the host star mass and distance, which could be obtained by combining our measurement of θ_E with a measurement of the lens light as outlined above. The Bayesian analysis informs the likelihood of success of such an endeavor. This analysis suggests that, if the host is a main-sequence star, its magnitude will be $I_L = 23.9^{+0.8}_{-1.0}$ and $H_L = 21.4^{+0.7}_{-1.0}$, which corresponds to 0.6% and 1.7% of the source flux, respectively. If initial efforts to detect the lens fail, more aggressive observations would certainly be warranted: microlensing is the most sensitive method for detecting planets around very low mass stars simply because it is the only method that does not rely on light from the host (or the planet itself) to detect the planet. And given Equation (6), even an M dwarf at the very bottom of the main sequence $M = 0.08\ M_\odot$, would lie at $D_L = 3.5$ kpc and so would be $H \sim 24$.

We thank Shude Mao, David Heyrovsky, and Pascal Fouque for useful comments during the completion of this work. S.D. and A.G. were supported in part by grant AST-0757888 from the NSF. S.D., A.G., D.D., and R.P. acknowledge support by NASA grant NNG04GL51G. A.G. thanks IAP, CNRS for its support. The MOA group acknowledge Ministry of Education, Culture, Sports, Science and Technology of Japan (MEXT and JSPS) no. 18253002 and 20340052 for support. I.A.B., J.B.H., P.M.K., D.J.S., W.S., P.C.M.Y. acknowledge Marsden Fund of NZ. D.P.B. was supported by grants AST-0708890 from the NSF and NNX07AL71G from NASA. L.S. is supported by NZ Foundation of Science, Research, and Technology. C.H. is supported by SRC Korea Science & Engineering Foundation. B.-G.P. acknowledges the support by Korea Astronomy & Space Science Institute. The OGLE project is partially supported by the Polish MNiSW grant N20303032/4275. This work was supported in part by an allocation of computing time from the Ohio Supercomputer Center.

APPENDIX

FAILURE OF ELLIPTICAL-SOURCE MODELS

Because MOA-2007-BLG-400 is the first microlensing event with a completely buried caustic, it is important to rule out other potential causes of the deviations seen in the light curve (apart from a planetary companion to the lens). The principal features of these deviations are the twin "spikes" in the residuals, which are approximately centered on the times when the lens enters and exits the source. In the model, these crossings occur at about $\mathrm{HJD}' = 4354.53$ and $\mathrm{HJD}' = 4354.63$, i.e., very close to the spikes in Figure 1. In principle, one might be able to induce such spikes by displacing the model source crossing times from the true times. The only real way to achieve this (while still optimizing the overall fit parameters) would be if the source were actually elliptical, but were modeled as a circle (which, of course, is the norm).

One argument against this hypothesis is the similarity of the I and H residuals (Section 3). If the source were an ellipsoidal variable, then one would expect color gradients due to "gravity darkening."

Nevertheless, we carried out two types of investigation of this possibility. First, we modeled the light curve as an elliptical source magnified by a point (nonbinary) lens. In addition to the linear flux parameters (source flux plus blended flux for each observatory) there are six model parameters, the three standard point-lens parameters (t_0, u_0, t_E), plus the source semimajor and semiminor axes (ρ_a, ρ_b) and the angle of the source trajectory relative to the source major axis, α. We find that the elliptical source reduces χ^2 by about 200, but it does not remove the "spikes" from the residuals, which was the primary motivation for introducing it. Instead, essentially all of the χ^2 improvement comes from eliminating the asymmetries from the rest of the light curve. Recall, however, that the planetary model removes both these asymmetries and the "spikes." Moreover, the best-fit axis ratio is quite extreme, $\rho_b/\rho_a = 0.7$, which would produce very noticeable ellipsoidal variations unless the binary were being viewed pole on.

Next, we looked for sinusoidal variations in the baseline light curve. The individual OGLE error bars at baseline are smaller than for MOA, and since ellipsoidal variations are strictly periodic, the longer OGLE baseline (about $T = 2000$ days versus $T = 800$ days for MOA) does a better job of isolating this signal from various possible systematics. Therefore, for this purpose, the OGLE data are more suitable than MOA. The OGLE data are essentially all baseline (only two magnified points out of 452). Their periodogram shows several spikes at the 0.01 mag level, and a maximum $\Delta\chi^2 = 20$, which are consistent with noise. The width of the spikes is extremely narrow, consistent with the theoretical expectation for uniformly sampled data of $\sigma(P)/P^2 \sim \sqrt{24/\Delta\chi^2}/(2\pi T) \sim 10^{-4}$ day^{-1}, indicating that the data set is behaving normally.

In brief, our investigation finds no convincing evidence for ellipticity of the source, certainly not for the several tens of percent deviation from circular that would be needed to significantly ameliorate the deviations seen near peak in the light curve. Moreover, even arbitrary source ellipticities cannot reproduce the light curve's most striking features: the two "spikes" in the residuals that occur when the lens crosses the source boundary.

REFERENCES

Albrow, M. D., et al. 2002, ApJ, 572, 1031
Alcock, C., et al. 2001, Nature, 414, 617
An, J., et al. 2002, ApJ, 572, 521
Beaulieu, J.-P., et al. 2006, Nature, 439, 437
Bennett, D. P., Anderson, J., & Gaudi, B. S. 2007, ApJ, 660, 781
Bennett, D. P., & Rhie, S. H. 1996, ApJ, 472, 660
Bennett, D. P., & Rhie, S. H. 2002, ApJ, 574, 985
Bennett, D. P., et al. 2008, ApJ, 684, 663
Bessell, M. S., & Brett, J. M. 1988, PASP, 100, 1134
Bond, I. A., et al. 2001, MNRAS, 327, 868
Bond, I. A., et al. 2002, MNRAS, 331, L19
Bond, I. A., et al. 2004, ApJ, 606, L155
Burrows, A., Hubbard, W. B., Saumon, D., & Lunine, J. I. 1993, ApJ, 406, 158
Burrows, A., et al. 1997, ApJ, 491, 856
Chang, K., & Refsdal, S. 1979, Nature, 282, 561
Chung, S.-J., et al. 2005, ApJ, 630, 535
Claret, A. 2000, A&A, 363, 1081
Cumming, A., Butler, R. P., Marcy, G. W., Vogt, S. S., Wright, J. T., & Fischer, D. A. 2008, PASP, 120, 531
Demarque, P., Woo, J.-H., Kim, Y.-C., & Yi, S. K. 2004, ApJS, 155, 667
Dominik, M. 1999, A&A, 349, 108
Dominik, M. 2006, MNRAS, 367, 669
Dong, S., et al. 2006, ApJ, 642, 842
Dong, S., et al. 2009, ApJ, 695, 970
Endl, M., Cochran, W. D., Kürster, M., Paulson, D. B., Wittenmyer, R. A., MacQueen, P. J., & Tull, R. G. 2006, ApJ, 649, 436
Gaudi, B. S., & Gould, A. 1997, ApJ, 486, 85
Gaudi, B. S., et al. 2008, Science, 315, 927
Gould, A. 2008, ApJ, 681, 1593
Gould, A., & An, J. H. 2002, ApJ, 565, 1381
Gould, A., & Loeb, A. 1992, ApJ, 396, 104
Gould, A., et al. 2006, ApJ, 644, L37

Griest, K., & Safizadeh, N. 1998, ApJ, 500, 37
Han, C. 2007, ApJ, 661, 1202
Han, C., & Gaudi, B. S. 2008, ApJ, 689, 53
Han, C., & Gould, A. 1995, ApJ, 447, 53
Ida, S., & Lin, D. N. C. 2005, ApJ, 626, 1045
Johnson, J. A., Butler, R. P., Marcy, G. W., Fischer, D. A., Vogt, S. S., Wright, J. T., & Peek, K. M. G. 2007, ApJ, 670, 833
Kennedy, G. M., & Kenyon, S. J. 2008, ApJ, 673, 502
Kennedy, G. M., Kenyon, S. J., & Bromley, B. C. 2006, ApJ, 650, L139
Kervella, P., Thévenin, F., Di Folco, E., & Ségransan, D. 2004, A&A, 426, 297
Kozłowski, S., Woźniak, P. R., Mao, S., & Wood, A. 2007, ApJ, 671, 420
Laughlin, G., Bodenheimer, P., & Adams, F. C. 2004, ApJ, 612, L73
Lecar, M., Podolak, M., Sasselov, D., & Chiang, E. 2006, ApJ, 640, 1115
Liebes, S. 1964, Phys. Rev., 133, 835
Lin, D. N. C., Bodenheimer, P., & Richardson, D. C. 1996, Nature, 380, 606
Lissauer, J. J. 1987, Icarus, 69, 249
Mao, S., & Paczynski, B. 1991, ApJ, 374, L37
Pejcha, O., & Heyrovský, D. 2009, ApJ, 690, 1772
Pollack, J. B., Hubickyj, O., Bodenheimer, P., Lissauer, J. J., Podolak, M., & Greenzweig, Y. 1996, Icarus, 124, 62
Rasio, F. A., & Ford, E. B. 1996, Science, 274, 954
Rattenbury, N. J., Bond, I. A., Skuljan, J., & Yock, P. C. M. 2002, MNRAS, 335, 159
Udalski, A., et al. 2005, ApJ, 628, L109
Ward, W. R. 1997, Icarus, 126, 261
Woźniak, P. R. 2000, Acta Astron., 50, 421
Yoo, J., et al. 2004, ApJ, 603, 139